Journal of Materials Chemistry A

Machine Learning Reveals Factors that Control Ion Mobility in Anti-Perovskite Solid Electrolytes

Journal:	*Journal of Materials Chemistry A*
Manuscript ID	TA-ART-05-2022-003613.R1
Article Type:	Paper
Date Submitted by the Author:	22-Jun-2022
Complete List of Authors:	Kim, Kwangnam; Lawrence Livermore National Laboratory, Meterials Science Division Siegel, donald; The University of Texas at Austin, Mechanical Engineering

Machine Learning Reveals Factors that Control Ion Mobility in Anti-Perovskite Solid Electrolytes

Kwangnam Kim[†#] and Donald J. Siegel[†, ‡, §, ||, Σ,#,*]

[†]Mechanical Engineering Department, [‡]Materials Science & Engineering, [§]Applied Physics Program, [||]University of Michigan Energy Institute, and [Σ]Joint Center for Energy Storage Research, University of Michigan, Ann Arbor, Michigan 48109-2125, USA

ABSTRACT: Solid-state batteries are projected to exhibit improved energy densities and safety compared to liquid-electrolyte-based systems. Consequently, the development of solid electrolytes that can conduct cations at rates comparable to that of liquid electrolytes is an active area of research. To facilitate this search it is desirable to understand the chemical and structural features that control ion transport through a crystalline lattice. Here, machine learning (ML) is used to identify features that influence ion mobility in solids, quantify the relative importance of those features, and demonstrate how the variation of individual features alters ion mobility. Adopting the anti-perovskite lattice as a model system, ML algorithms were trained to predict migration barriers from a data set containing hundreds of barriers calculated using density functional theory. More than 10^6 feature sets of non-redundant descriptors were evaluated for their ability to predict migration barriers. The present analysis correctly reiterates the importance of several features that are known to influence mobility – for example, anion polarizability – but also identifies others whose importance is not widely recognized. Lattice properties such as hopping distance and channel width exhibit the greatest influence on cation mobility. Individual conditional expectation analyses performed on these features shows that barriers decrease as hopping distance decreases and as channel width increases. The defect formation energy – which is commonly associated with the concentration of defects, but not with their mobility – is identified as an important feature for interstitial migration. In sum, this analysis aids in the design of optimal solid electrolytes by simplifying the multi-dimensional design space to a sub-set of properties that are the most important.

INTRODUCTION

Li-ion batteries (LIBs) have achieved wide-spread use in applications ranging from portable electronics to grid-scale energy storage.[1] Despite this success, further improvements in the performance of LIBs are desirable, an important example being their safety. One way to enhance safety is to replace the flammable and volatile liquid electrolytes used in present LIBs with a solid electrolyte (SE).[1–3] An additional benefit of a SE-based battery derives from the high stiffness of some SEs, which may allow for use of a Li-metal anode in place of graphitic carbon. This substitution would increase energy density.[4,5]

Although an increasing number of materials have been suggested as SEs,[6–12] many are not stable with Li metal, have small electrochemical windows, or are susceptible to dendrite penetration at practical current densities.[13–16] Hence, new SE compositions may be needed to realize the benefits of solid-state Li-metal batteries.

To design suitable SEs it is desirable to understand which fundamental properties (or 'features') control ion mobility in solids. Several features that may impact ion transport have been described in the literature. For example, the frequencies and amplitudes of phonons have been proposed to influence ion mobility.[17,18] Chemical features such as the polarizability of atoms have also been proposed to correlate with ion migration.[19–23] The structure of the crystalline lattice can also play a role: migration barriers have been reported to increase for coordination geometries that increase the stability of the cation site.[24] Low energy barriers can be achieved by adopting a bcc anion sublattice, which allows for direct hopping between tetrahedral sites.[25] Volume effects have also been discussed: larger cell volumes resulting from the use of larger anions tend to decrease migration barriers by widening the size of the migration channel.[25–27] (Note that larger anions are also more polarizable.)[28] Solids having relatively low densities, such as high-temperature polymorphs and glasses, have been reported to exhibit enhanced ionic conductivity arising from 'paddlewheel' dynamics.[29–36] Finally, lattice distortions introduced by mis-matched atom sizes can lower the barriers associated with a subset of migration ion pathways.[37]

Although several studies have examined features that impact ion mobility in solids, the *relative importance* of these features has not been examined in detail. Furthermore, additional features that correlate with ion mobility may exist that have not yet been brought to light. Finally, multiple features may impact ionic mobility simultaneously.[38] Consequently, a mechanism for systematically identifying and assessing the importance of various features on ion mobility would be helpful. Such an approach would facilitate the design of new SEs by reducing the multi-dimensional feature space to a sub-set of properties that are the most important.

Machine learning (ML) provides a mechanism to accomplish these goals. ML can identify complex relationships between features and a target property.[39] In prior work, ML was used to screen for new superionic conductors.[40–46] In the taborite system,

Jalem et al. showed that structural features are the most important features to decrease migration barriers using neural network and Gaussian processing models.[42,45] Sendek et al. suggested several features that can be used to classify ionic conductors: Li-anion distance, Li-Li distance, ionicity, anion coordination, and Li coordination.[44] Also, Katcho et al. trained a random forest model on migration barriers from Li and Na oxides (predicted by the bond-valence method). They showed that the channel size, cation-anion coordination number, and the volume fraction of the cation are important features.[46]

This present study uses ML to quantify the importance of several chemical, physical, and structural features on ion transport within a crystalline lattice. Adopting the anti-perovskite (AP) crystal structure as a model system, several ML algorithms were trained to predict ion migration barriers. The algorithms were informed from a data set containing more than 300 barriers that were calculated using density functional theory. The training set is derived from 36 alkali metal chalco-halide anti-perovskites, and includes vacancy and interstitial migration mechanisms.[37,47] Highly correlated (i.e., redundant) features were identified and eliminated, thus maximizing the simplicity of the resulting models and minimizing overfitting. Using the most accurate algorithm, the feature combinations that yielded the most accurate predictions were identified. Finally, the relative importance of the features and their influence on ion transport were quantified using the mean decrease in impurity (MDI) and individual conditional expectation (ICE) plots.

This analysis reveals that lattice properties such as hopping distance and channel width have the greatest influence on cation mobility. These features comprise 70% of the total feature importance for vacancy migration, and ~50% of the importance for interstitial migration. Individual conditional expectation analyses performed on these features show that barriers decrease as hopping distance decreases and as channel width increases. Additional significant features include the anion polarizability (22% for vacancy migration) and the defect formation energy (35% for interstitial migration). The identification of the interstitial formation energy as a significant feature is noteworthy, and perhaps unexpected, because this feature is well-known to control the concentration of defects, but it is not widely recognized as one that influences mobility. In sum, this feature importance analysis facilitates the design of efficient solid electrolytes by reducing the multi-dimensional design space to a sub-set of properties that are the most impactful. An additional benefit derives from the fact that many of the identified features are elementary properties that are tabulated or are straightforward to evaluate, thus further simplifying the discovery process.

METHODS

The *scikit-learn* ML package was adopted for this study.[48] Figure 1 summarizes the computational workflow. The workflow consists of four stages: (1) In the *Data* stage hundreds of migration barriers and 44 features were assembled and evaluated (the complete dataset, including all descriptors and their associated migration barriers, is provided in the Supporting Information); (2) *Feature filtering* was subsequently used to eliminate highly correlated (redundant) features; (3) Next, in the *ML model selection* stage, 18 ML algorithms were trained, optimized, and assessed for to their ability to predict migration barriers; (4) In the last stage, *Feature subset evaluation*, the features that most strongly impact migration barriers were determined.

Migration barrier data. The elementary migration barriers for cations in 36 model alkali metal-chalcohalide APs with formula X_3AZ (where X = Li, Na, or K, A = O, S, or Se, and Z = F, Cl, Br, or I), were adopted from self-consistent set of DFT calculations.[37,47] In the AP system the cation (X) sublattice consists of vertex-sharing octahedra. The smaller chalcogen anion (A) typically occupies the octahedron center, while the larger halogen anion sits at the vertices of a cubic framework.[37,49] Cation migration occurs along pathways that correspond to the edges of the octahedra. Due to their high symmetry, cubic APs have one unique migration pathway (i.e., all pathways along the octahedron edges are identical), whereas 12 unique paths exist in the lower-symmetry orthorhombic systems (due to tilting of the alkali-metal octahedra), corresponding to the 12 edges of the octahedra. Energy barriers were evaluated for both vacancy and interstitial dumbbell migration mechanisms. (Details of the calculation methods, migration mechanisms, and distribution of the barrier energies are provided in Ref. [37,47,50].)

A total of 603 barriers were evaluated, including 322 and 281 for vacancy and interstitial mechanisms, respectively. This quantity of data satisfies the guideline that the amount of training data should exceed the number of descriptors by approximately a factor of five.[51] This guideline has been proposed as a means avoid the 'curse of dimensionality' (i.e.,

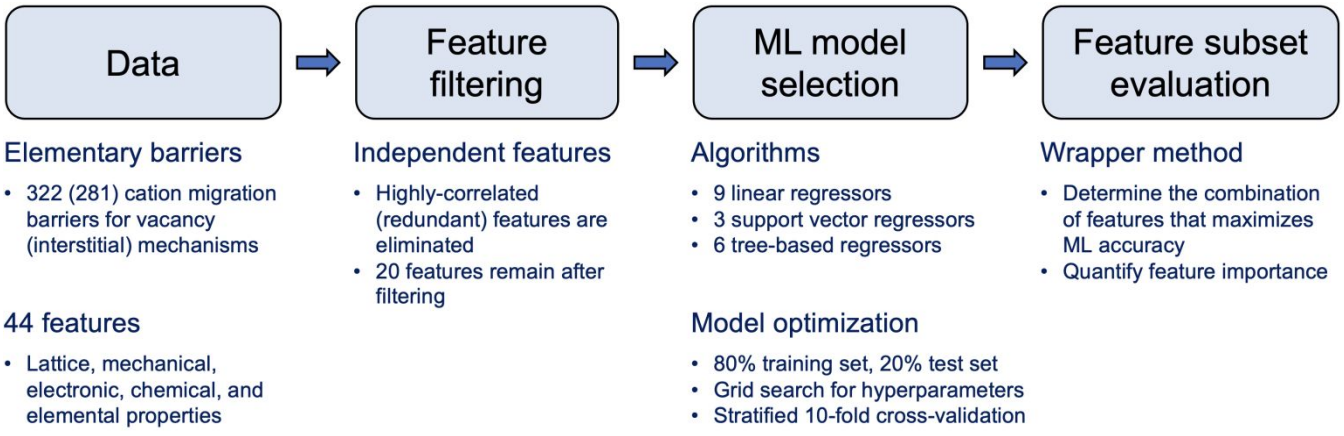

Figure 1. Machine learning workflow used to identify features that influence ion migration barriers in anti-perovskite SEs.

Table 1. List of descriptors examined in this study, their categories, and whether a given descriptor was eliminated due to a high correlation with another descriptor.

Descriptor	Category	Redundant descriptor
Unit cell volume per atom (V_a)	Lattice	
Octahedron volume (V_{octa})	Lattice	V_a
Mass density (ρ_m)	Lattice	
Packing fraction of anions (PF_A)	Lattice	PW
Tolerance factor (t)	Lattice	
Channel size (D_i)	Lattice	PW
Coordination number of cation (CN_C)	Lattice	
Path distance (CCD)	Lattice	
Cation – octahedral anion distance (COD)	Lattice	CCD
Cation – framework anion distance (CFD)	Lattice	AAD
Distance between anions (AAD)	Lattice	CCD
Path width as determined by perpendicular distance to closest ion (PW_c)	Lattice	PW
Path width as determined by perpendicular distance to 2nd closest ion (PW_{2c})	Lattice	PW
Total path width (PW)	Lattice	
Phonon frequency (ω_{LEO})	Lattice	B
Bulk modulus (B)	Mechanical	V_a
Band gap (E_g)	Electronic	B
Electronic dielectric constant (ε_e)	Electronic	
Ionic dielectric constant (ε_i)	Electronic	
Total dielectric constant (ε)	Electronic	ε_i
Polarizability ($\overline{\alpha}$)	Electronic	V_a
Ionic radius (r_C)	Cation	α_C
Atomic mass (m_C)	Cation	α_C
Electronegativity (EN_C)	Cation	α_C
Ion polarizability (α_C)	Cation	
Bader charge (BC_C)	Cation	
Born effective charge (BEC_C)	Cation	
Ionic radius (r_O)	Octahedral anion	α_O
Atomic mass (m_O)	Octahedral anion	α_O
Electronegativity (EN_O)	Octahedral anion	α_O
Ion polarizability (α_O)	Octahedral anion	
Bader charge (BC_O)	Octahedral anion	
Born effective charge (BEC_O)	Octahedral anion	
Ionic radius (r_F)	Framework anion	α_F
Atomic mass (m_F)	Framework anion	α_F
Electronegativity (EN_F)	Framework anion	α_F
Ion polarizability (α_F)	Framework anion	
Bader charge (BC_F)	Framework anion	
Born effective charge (BEC_F)	Framework anion	BEC_O
Bond ionicity between cation and chalcogen anion ($I_{C\text{-}Ch}$)	Chemical	
Bond ionicity between cation and halogen anion ($I_{C\text{-}H}$)	Chemical	
Bond ionicity between anions ($I_{Ch\text{-}H}$)	Chemical	$I_{C\text{-}H}$
Decomposition energy (E_d)	Chemical	
Defect formation energy (E_f)	Chemical	

overfitting).[52] Importantly, the dataset includes a mixture of low- and high-barrier pathways: barriers range from 38 to 847 meV for vacancy migration and from 12 to 382 meV for the interstitial dumbbell mechanism. This diversity of data will improve the reliability of the ML models.[51] Furthermore, all of the barrier data are evaluated using the same simulation method. This consistency presents advantages compared to approaches that mix data from several sources and/or incorporate experimental data. In the latter case, experimentally-measured activation energies can include contributions from grain boundaries or other defects that complicate comparisons. Here, the focus is solely on migration barriers.

Descriptors. 44 descriptors with the potential to influence ion mobility were considered, Table 1. The descriptors were categorized into five groups based on the nature of the feature: 'lattice', 'mechanical', 'electronic', 'chemical', or 'elemental.' The first 4 of these categories refer to properties of the AP compound. The latter category refers to properties of the

individual cations and anions. The descriptors include information about the local atomic environments associated with each elementary migration path, thus allowing individual paths to be differentiated. Descriptor values were adopted from tabulated data or from DFT calculations on the APs.[37,47,50] The polarizability of a compound was calculated using the Clausius-Mossotti relation:[53]

$$\overline{\alpha} = \frac{3}{4\pi}\left(\frac{\varepsilon_e - 1}{\varepsilon_e + 2}\right)V_{\mathrm{a}},$$

where ε_e is the electronic dielectric constant and V_a is the unit cell volume per atom. Additional details about the calculation methods[17,18,55–64,22,65,66,26,37,44,47,50,53,54] are provided in the Supporting Information.

Although the feature set employed here is intended to include essentially all elementary properties that could impact ion mobility in solids, one cannot rule out the possibility that the feature set remains incomplete due the omission of "unknown unknowns" – i.e., features that are significant and should be included, yet are absent due to gaps in our understanding. An additional opportunity for improvement would be to include features that capture dynamical phenomena. The present feature set emphasizes static properties; these features have the advantage that some are known to influence ion mobility in some systems; furthermore, they are straightforward to calculate and/or are tabulated in standard references. Thus, static properties are a reasonable and maximally-simple starting point. Nevertheless, several studies have pointed to the importance of dynamic phenomena in understanding ion mobility. These include the vibrational properties of the lattice and the rotational properties of complex anions (i.e., a paddlewheel effect).[29–36] While anion rotations are not relevant for the present set of anti-perovskites, a more complete (but more expensive to evaluate) feature set would include dynamical properties.

Feature filtering. Filtering was used to reduce the dimensionality of the feature space by eliminating highly-correlated (redundant) descriptors. By reducing the number of features, filtering minimizes both the computational expense of the ML model and the risk of overfitting. Potential relationships between descriptors were assessed by evaluating their Pearson correlation, $\rho_{\mathrm{X,Y}}$:[67]

$$\rho_{\mathrm{X,Y}} = \frac{cov(\mathrm{X,Y})}{\sigma_{\mathrm{X}}\sigma_{\mathrm{Y}}},$$

where cov(X,Y) is the covariance of features X and Y and $\sigma_{\mathrm{X\ or\ Y}}$ is the standard deviation of feature X or Y. $\rho_{\mathrm{X,Y}}$ measures the degree of linear correlation between features X and Y, and has a range $-1 \leq \rho \leq 1$. Here, 0 implies no correlation and ± 1 represents a perfect positive/negative correlation. Redundant descriptors were defined as those with $|\rho| \geq 0.80$. In the case of correlated features, only one of the correlated descriptors was retained in the feature set; the other feature(s) were removed. An example of a correlated pair of features is the unit cell volume per atom (V_a) and polarizability ($\overline{\alpha}$) (ρ = 0.97). This correlation is expected since the polarizability of an atom or ion scales with its 'size.'[28] From these redundant feature subsets, the feature that was retained for use in the ML analysis was selected based on a combination of: (a) the ease of evaluating the descriptor, and (b) a desire to reflect existing knowledge from the literature, when appropriate. Additional details regarding feature filtering are provided in the SI.

Model selection. 18 ML algorithms were examined with the goal of identifying the one that predicted migration energies most accurately. These algorithms included 9 linear regressors, 3 support vector regressors (SVRs), and 6 tree-based regressors. A summary of the algorithms[51,68,77–86,69–76] explored is provided in the Supporting Information.

The dataset of migration barriers was randomly divided into a training set (80% of the data) and a test set (20%). As needed, this random division was repeated until the two sets exhibited similar distributions of barriers as measured by the mean and standard deviation. The mean and standard deviation of the training set were 262 and 136 meV, respectively, while those of test set were 268 and 145 meV, respectively. Hyperparameter optimization was performed using a grid search with stratified 10-fold cross-validation (CV). Training samples were divided into 10 validation sets evenly so that the maximum difference between the mean target values of the validation sets was less than 10% of the mean target value of the entire training set (i.e., stratified). Literature reports have shown that although 10-fold CV is a reasonable choice, stratification is generally a better scheme than a regular CV for both bias and variance, and that stratified 10-fold CV may be better than more expensive leave-one-out CV for model optimization.[87] The test set was not involved in the model optimization process, but was used to estimate the prediction performance of the optimized model from each algorithm after training. The model with the smallest error was used to evaluate feature subsets.

Feature subset evaluation. The 'wrapper' method was used to identify the subset of features that result in the most accurate ML models for a specified number of features, n.[88] Like filtering, the wrapper method is an example of feature selection. Unlike filtering, it proceeds via repeatedly selecting distinct subsets of features and training a given ML algorithm with those feature sets. With 20 descriptors remaining in the feature set after filtering (see discussion below), $\sum_{n=1}^{20}\binom{20}{n}$ = 1,048,575 n-feature sets were evaluated. The most predictive feature set was determined based on the accuracy of its resulting ML model. Notably, the case of n = 1 allows one to answer the question: "what is the most important single feature for predicting ion migration barriers?"

Feature importance and influence on barriers. A goal of the present study is to evaluate the relative importance of features on the size of ion migration barriers. This is straightforward for linear regression models that explicitly show the importance via their coefficients, but is more complicated for models such as neural networks, SVM, tree models, etc. These algorithms are often referred to as 'black box' models because they are not directly interpretable.[86]

As described below, a tree-based algorithm was found to be the most accurate model for predicting migration barriers. For tree-based algorithms feature importance can be quantified with the mean decrease in impurity, MDI. MDI is defined as the total decrease in impurity (for classification models) or variance (for regression models) contributed by a certain feature:[78]

$$MDI(x) = \sum_i [n_i var_i(x) - (n_{LL} var_{LL}(x) + n_{RL} var_{RL}(x))].$$

Here, the sum is over nodes i split by a feature x, n is the number of samples in a node i and its left and right leaves (denoted as subscripts LL and RL, respectively), and var is the variance of target values of samples in the node and leaves. MDI measures how much a feature contributes to minimizing the variance by

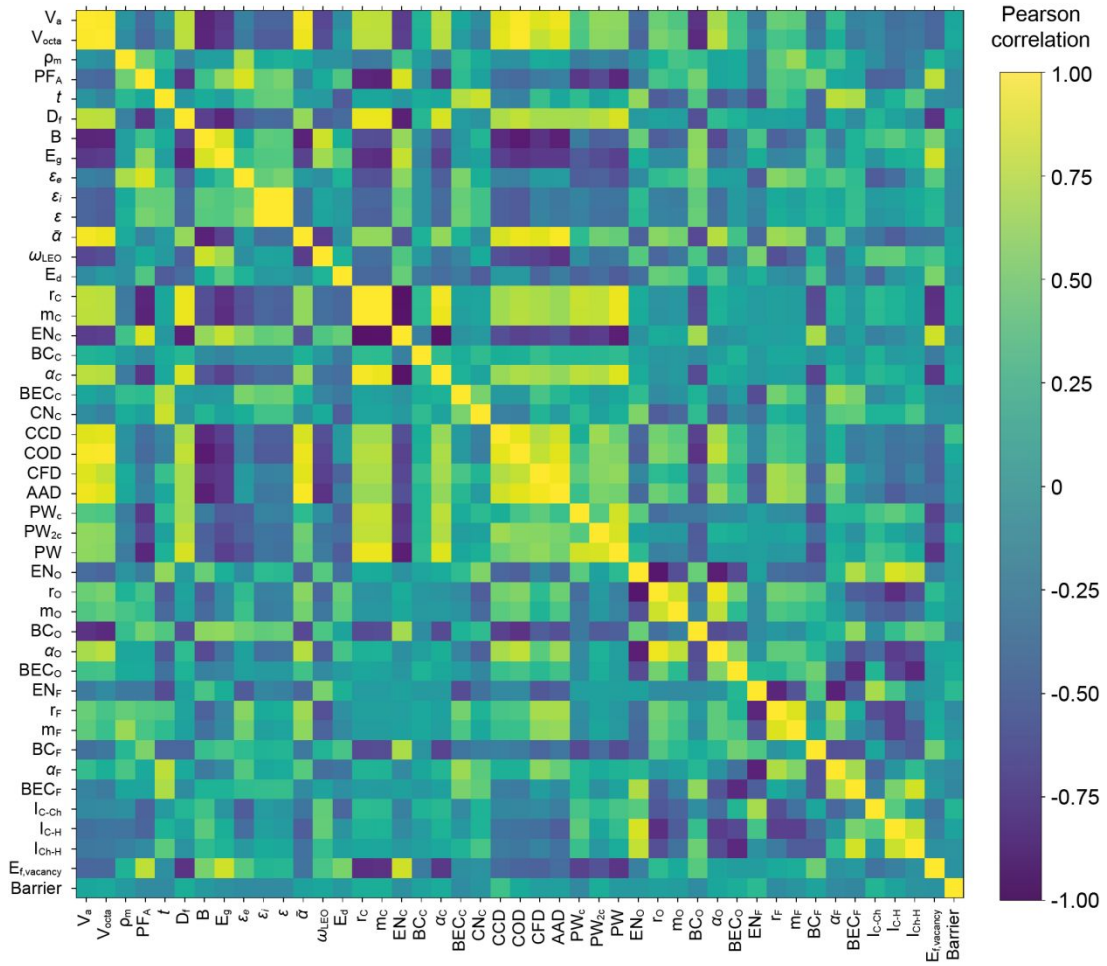

Figure 2. Pearson correlation analysis for descriptors and vacancy migration barriers.

node division throughout the tree model. Features with larger MDI values are more important.

Although MDI can evaluate *if* a given feature is important, it does not describe *how* a feature affects a target property. For example, MDI can evaluate if 'path distance' is important, but cannot identify whether longer path distances increase or decrease the migration barrier. In contrast, the individual conditional expectation (ICE) plot can quantify how changing an individual feature changes the target property.[86,89] The ICE plot illustrates the variation in the predicted target value (i.e., size of the migration barrier) using *conditional expectation curves* generated from the training data.[89] A conditional expectation curve is created using the optimal ML model for each set of features that corresponds to a given AP composition and migration path in the training set. [The number of curves in the ICE plot is equal to the number of data points (i.e., barriers) contained in the training set.] The feature whose impact is to be determined is varied, and the values of all other features are held fixed. ICE plots were constructed such that the migration barrier is assigned a value of zero when the selected feature adopts its minimum value within the training set. This convention is known as a 'centered' ICE plot; this approach makes explicit how the barrier varies as the value of the selected feature increases. ICE analysis was performed using the *PDPbox* package.[90]

RESULTS AND DISCUSSION

Feature filtering. Figure 2 illustrates the matrix of Pearson correlation coefficients (ρ) for descriptors used to predict migration barriers via the vacancy mechanism. The calculated migration barriers are included in the correlation analysis as the last row and column in the matrix. (Data used to generate Figure 2 is provided in the Supporting Information.) Looking first at the correlations between features and the barriers, it is observed that no single feature exhibits a high correlation with the barrier – the largest correlation, ρ= 0.34, is obtained for the path distance, CCD. A similar result was obtained for the dumbbell mechanism, where a max correlation of 0.14 is calculated between the barrier and the phonon frequency, ω_{LEO}, see Figure S1. This confirms that linear correlations involving a single feature do not strongly correlate with ion migration in the APs. In contrast, and as shown below, ML successfully identifies more complex connections between features and migration barriers.

Table 1 also identifies twenty-four redundant features that were eliminated from the feature set in favor of other features with which they exhibit strong correlations, $|\rho| \geq 0.80$. For example, the band gap (E_g) and phonon frequency (ω_{LEO}) correlate to the bulk modulus (B) with ρ = +0.85 and +0.81, respectively. Also, the volume of the unit cell per atom (V_a) correlates strongly with the volume of the cation octahedra

(V_{octa}, ρ = +0.98), polarizability ($\overline{\alpha}$, ρ = +0.97), and bulk modulus (B, ρ = -0.88). Consequently, the descriptors V_{octa}, $\overline{\alpha}$, B, E_g, and ω_{LEO} were dropped in favor of retaining V_a, since the latter is straightforward to calculate. As expected, the total dielectric constant (ε) is strongly correlated with the ionic dielectric constant (ε_i), ρ = +0.99, because the ionic contribution to the total dielectric constant is observed to be much larger than the electronic contribution (ε_e) in APs.[47,50] Hence, ε_i was retained and ε was removed.

Regarding properties of the ions, the ionic radius, atomic mass, electronegativity, and ion polarizability of each species are highly correlated, as expected. For example, in the case of cations, the ion polarizability (α_C) correlates strongly with the ionic radius (r_C, ρ = +0.96), the atomic mass (m_C, ρ = +0.94), and the electronegativity (EN_C, ρ = -0.98). Similar correlations hold for the anions. Based on these correlations, the ionic radius, atomic mass, and electronegativity were dropped in favor of retaining ion polarizability. (Although the former three features are more straightforward to obtain than the latter, anion polarizability has previously been discussed as a parameter that impacts conductivity in SEs, and was thus retained to maintain consistency with the extant literature.[19–23]) The Born effective charge of the octahedral anion (BEC_O) correlates with that of the framework anion (BEC_F), ρ = -0.85; hence, BEC_F was eliminated in favor of retaining BEC_O. [We note that the Pearson correlation between the Bader charges and Born effective charges is moderate for anions (ρ = -0.62) and weak for cations (ρ = +0.15). The absence of a strong correlation between these two measures of local charge may arise from the stronger sensitivity of the Bader charge to the local environment, and the relative insensitively of the Born charges to the same. A full tabulation of these charges is provided in the Supporting Information.]

Regarding geometric properties of the lattice, the path distance for cation migration (CCD, the linear distance between cation sites) correlates with the distance between cations and octahedral anions (COD, ρ = +0.91). CCD also correlates with anion-anion distances (AAD, ρ = +0.82), while AAD correlates with cation – framework anion distances (CFD, ρ = +0.96). Consequently, COD, AAD, and CFD were dropped in favor of retaining CCD. The total path width (PW, the sum of PW_c and PW_{2c}) correlates strongly with 4 descriptors: the path width determined by the perpendicular distance to the closest ion

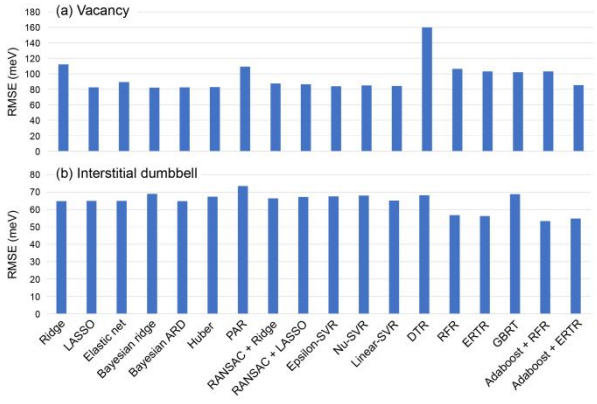

Figure 3. Comparison of the accuracy of ML models for predicting migration barriers for (a) vacancy and (b) interstitial dumbbell mechanisms.

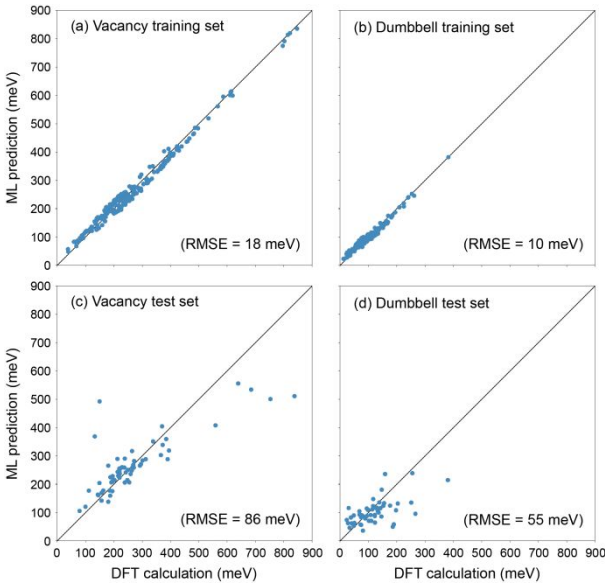

Figure 4. Comparison of ML predictions of migration barriers (adaboost + ERTR algorithm) with DFT calculations.

(PW_c, ρ = +0.83), the path width determined by the second closest ion (PW_{2c}, ρ = +0.86), the channel size (D_i, ρ = +0.85), and the anion packing fraction (PF_A, ρ = -0.87). All these descriptors relate to the space available for cation migration. Hence, PW_c, PW_{2c}, D_i, and PF_A were removed in favor of retaining PW.

Regarding chemical properties, the bond ionicity between cations and halogen anions ($I_{C\text{-}H}$) correlates with the bond ionicity between anions ($I_{Ch\text{-}H}$), ρ = +0.81; hence $I_{Ch\text{-}H}$ was removed in favor of retaining $I_{C\text{-}H}$. The latter term was retained based on the expectation that bond interactions between cations and anions are more relevant for predicting cation migration than are those between anions.

In total, the correlation analysis for vacancy migration resulted in the elimination of 24 redundant descriptors, with 20 descriptors retained. A similar result, with identical retained features, was obtained for the interstitial mechanism, Figure S1.

Model selection. Using the reduced feature set, 18 ML algorithms were optimized and evaluated with respect to their predictive accuracy on the training data set, Figure 3. For the vacancy migration mechanism, most of the linear regressors, SVRs, and 'adaboost + ERTR' algorithms exhibit good accuracy [exceptions include ridge and passive-aggressive regression (PAR)], with root mean squared errors (RMSE) of 82 to 89 meV. For the interstitial mechanism, tree-based regressors exhibit good accuracy [exceptions include the decision tree regressor (DTR) and gradient boosting regression tree (GBRT)] with RMSE of 53 to 57 meV. In total, the 'adaboost + ERTR' algorithm yielded good accuracy for both migration mechanisms; this algorithm exhibits the lowest summed RMSE over both the vacancy and interstitial mechanisms. Therefore, the 'adaboost+ ERTR' algorithm was adopted for use in the remainder of this study.

Figure 4 compares the migration barriers predicted by the 'adaboost + ERTR' ML algorithm (with input from the 20 non-redundant features) to those calculated by DFT. Figures 4a-b show comparisons for the training data for vacancy and

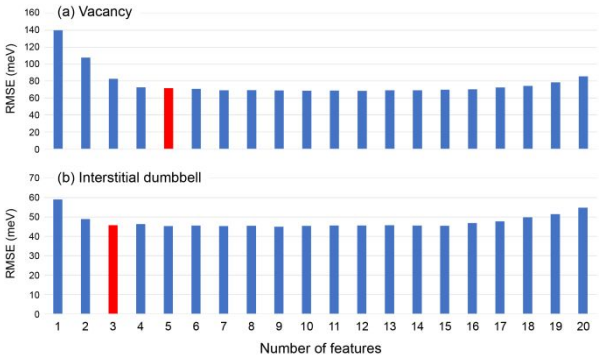

Figure 5. Comparison between the 'adaboost + ERTR' models with different numbers of features for (a) vacancy and (b) interstitial dumbbell mechanisms. Each bar represents the lowest RMSE for predicting the test data among models with different feature subsets for a fixed number of features. The red bar indicates the optimal number of features.

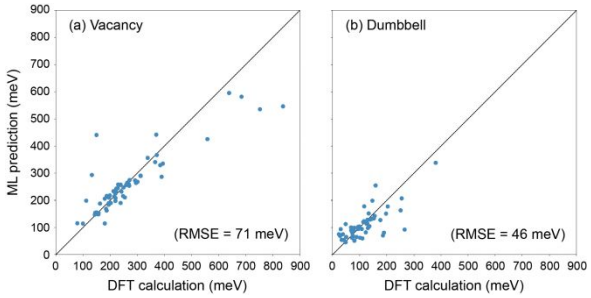

Figure 6. Performance of the adaboost + ERTR ML model relative to DFT calculations using the optimal feature sets shown in Fig. 5. (a) vacancy migration barriers predicted using five-features, and (b) dumbbell migration barriers predicted using three features.

interstitial mechanisms, respectively, while Figs. 4c-d show similar comparisons for the test set data. Overall, the agreement between ML and DFT is satisfactory for both the training and test data. In the case of the test set, the root mean squared error, RMSE, is 86 meV for the vacancy mechanisms and 55 meV for the interstitial mechanism. In the case of vacancy migration, a large portion of the RMSE derives from five data points having barriers larger than 550 meV; 48% of the sum of squared error (SSE) originates from these 5 samples. This error can be traced to the presence of limited data with barriers over 550 meV in the training set (~4% of the training set, Figure 4a). In the case of interstitial migration, a large portion of RMSE in the test set predictions derives from 8 data points with barriers larger than 180 meV; 70% of the SSE originates from these samples. As was the case for the vacancy training data, only 5% of the interstitial training data have barriers over 180 meV (Figure 4b), suggesting that additional training data would be helpful in predicting these high-barrier cases.

Feature subset evaluation. To determine the number and combination of features that yields the most accurate ML predictions, ML models were built using all possible subsets of the 20 non-redundant features. Figure 5 plots the RMSE for test set predictions for the most accurate resulting models as a function of the number of features used, n. (Tables S1 and S2 summarize the combination of features that minimize the RMSE for each value of n.) In the case of the vacancy mechanism, Fig. 5a, the RMSE initially decreases with n until a minimum RMSE of 71 meV is reached at n = 5. The RMSE is nearly constant for n = 5 to 15 before increasing for larger n. Such a 'U-shaped' trend is a well-known example of overfitting.[51] A similar trend is observed for the predictions of interstitial migration barriers: the RMSE initially decreases to a minimum at n = 3 (RMSE = 46 meV), remains roughly constant up to n = 15, and then increases again thereafter. It is noteworthy that the optimal ML models employ feature sets with fewer features – 5 features for vacancy migration, 3 for interstitial migration – than were used in the full 20-feature models, yet the former models exhibit superior accuracy. For example, the scatter plot in Figure 6 shows that the 5-feature model for vacancy migration has RMSE = 71 meV, whereas the 20-feature model has RMSE = 86 meV. In the case of interstitial migration, the RMSE is reduced from 55 meV in the 20-feature model to 46 meV in the 3-feature model. In addition to their improved accuracy, a further benefit of the reduced-feature models is their simplicity: models that rely on less input data are more easily interpreted, and are therefore more helpful in improving one's understanding.

In the spirit of improved understanding, it is instructive to consider the ML models constructed using only a single feature. The accuracy of these models is summarized in Figure S2 as a function of the feature employed. Although these models are less accurate than the multi-feature models (Fig. 5), they have the advantage of addressing the question: "if one is restricted to a single feature, which feature is most important?" In the case of vacancy migration, Fig. S2a indicates that V_a, the unit cell volume per atom, yields the most accurate predictions. This result seems reasonable when one recognizes that V_a is an information-rich descriptor: a larger V_a implies a longer migration distance, wider migration channel, and larger polarizability. These same factors have an impact on the vacancy migration barrier, as shown in the multi-feature importance analysis discussed below. Furthermore, since V_a is strongly correlated with the polarizability, $\bar{\alpha}$, and the bulk modulus, B, (Table 1) it can be concluded that the electronic and elastic "softness" of the SE are also relevant properties that are accounted for by the appearance of V_a.[19–23] In the case of interstitial migration (Fig. S2b), the formation energy, E_f, was identified as the single descriptor with the smallest error. This feature also appears in the multi-feature importance analysis, and will be discussed in more detail below.

Feature importance – vacancy migration. Using the mean decrease in impurity (MDI), Figure 7 illustrates the relative importance the features used by the reduced-feature ML models. Figure 7a illustrates feature importance for the vacancy mechanism. In this case, properties related to the crystal lattice – the path distance (measured by the cation-cation distance, CCD) and total path width (PW) – have the greatest impact on migration barriers; together, these two properties comprise 70% of the total importance. Path distance, with an importance of 42%, is the most impactful feature overall. Features that are strongly correlated with CCD, which were dropped during feature filtering, include: cation – octahedral anion distance (COD), cation – framework anion distance (CFD), and the anion-anion distance (AAD). Path distance, PW, with an importance of 28%, is the 2nd-most impactful feature overall. Features that are strongly correlated with PW, which were

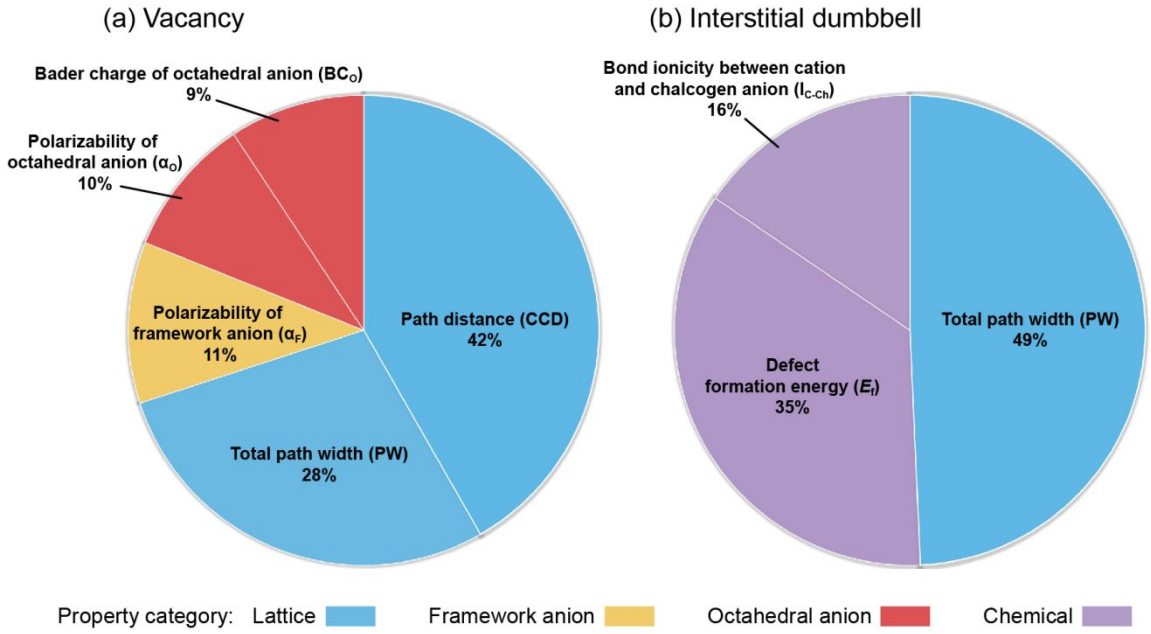

Figure 7. Relative importance of features used in ML models for ion migration via (a) vacancy and (b) interstitial mechanisms. Feature importance was assessed using the mean decrease in impurity. Colors distinguish the feature categories, which are defined in Table 1.

dropped during feature filtering, include: PW_c, PW_{2c}, D_i, and PF_A. It is noteworthy that CCD, PW, and all their correlated properties convey information related to the amount of 'free space' available for cation motion through the crystal lattice. Hence, one may conclude that lattice structure is the most important factor in determining ion mobility via a vacancy mechanism.

The next-most-important category of features for vacancy migration, comprising the remaining 30% of feature importance, are all related to the electronic properties of the anions. This group includes the polarizabilities of the framework anion (α_F, 11%) and the octahedral anion (α_O, 10%), and the Bader charge of the octahedral anion (BC_O, 9%). Correlations between anion polarizability and cation migration have been reported in the literature.[19–23] Anions that are more polarizable more readily allow for deformation of their electron clouds, and this deformation can facilitate cation migration. Redundant features that strongly correlate with polarizability include ionic radius (r), atomic mass (m), and electronegativity (EN). The Bader charge measures the net charge on an atom; thus BC_O reflects the degree of charge transfer from the cations to the octahedral anions. The Bader charge exhibits a moderate Pearson correlation with an ion's polarizability (ρ = -0.67 for BC_O and α_O and ρ = -0.63 for BC_F and α_F). As all of α_F, α_O, BC_O, and their redundant/correlated features are intrinsic properties of the respective anions, we conclude that the choice of the anions (or composition of the SE) is the 2nd-most-important factor in influencing vacancy-mediated ion migration.

Figure 8 shows ICE plots for the five features used in the ML model for vacancy migration. These plots quantify how changing one of these features (while keeping all others constant) changes the barrier value. Figure 8a shows the dependence on path distance; increasing the path distance increases the barrier. Hence, shorter migration distances are desirable for enhancing cation mobility. Notably, the magnitude of the average increase in the barrier (shown by the bold line in Fig. 8) from smallest to largest CCD is nearly 400 meV. This is the largest change in the barrier for any of the 5 features shown in the ICE plots. The high sensitivity of the barrier to CCD is consistent its high importance as determined by the MDI, Fig. 7a. A previous ML study also reported that the average distance between mobile ions is a useful feature for classifying superionic conductors.[44]

Figure 8b shows that the migration barrier decreases with increasing PW, implying that wider migration channels are beneficial for facile ion transport. The magnitude of the change in barrier height is approximately 200 meV over path widths ranging from 0.21 to 2.17 Å. This degree of barrier variation is roughly half that observed for CCD, yet is larger than that for the remaining three features in Figures 8c-e. Hence, this behavior is consistent with PW being the second-most important feature based on MDI, Fig. 7a.

Figure 8c shows that the barrier height decreases (in a step-wise fashion) with increasing polarizability of the framework anion, α_F. The three leftmost data points corresponding to small α_F values originate from fluorine ions in different anti-perovskite environments: K_3OF (α_F = 0.89), Na_3OF (α_F = 1.02), and Li_3OF (α_F = 1.20). Systems with this degree of polarizability for the framework anions have the highest migration barriers compared to other APs containing other framework anions (i.e., Cl, Br, I, S, and Se). For larger α_F the energy barrier initially decreases by ~100 but then plateaus for larger polarizabilities. Figure 8d also shows an overall decrease in the barrier with increasing polarizability of the octahedral anion, α_O. This decrease is preceded by a small increase in the barrier at small α_O corresponding to polarizabilities typical of fluorine ions. Overall, these results demonstrate that the migration barrier decreases with increasing polarizability of the anions, as proposed in earlier studies.

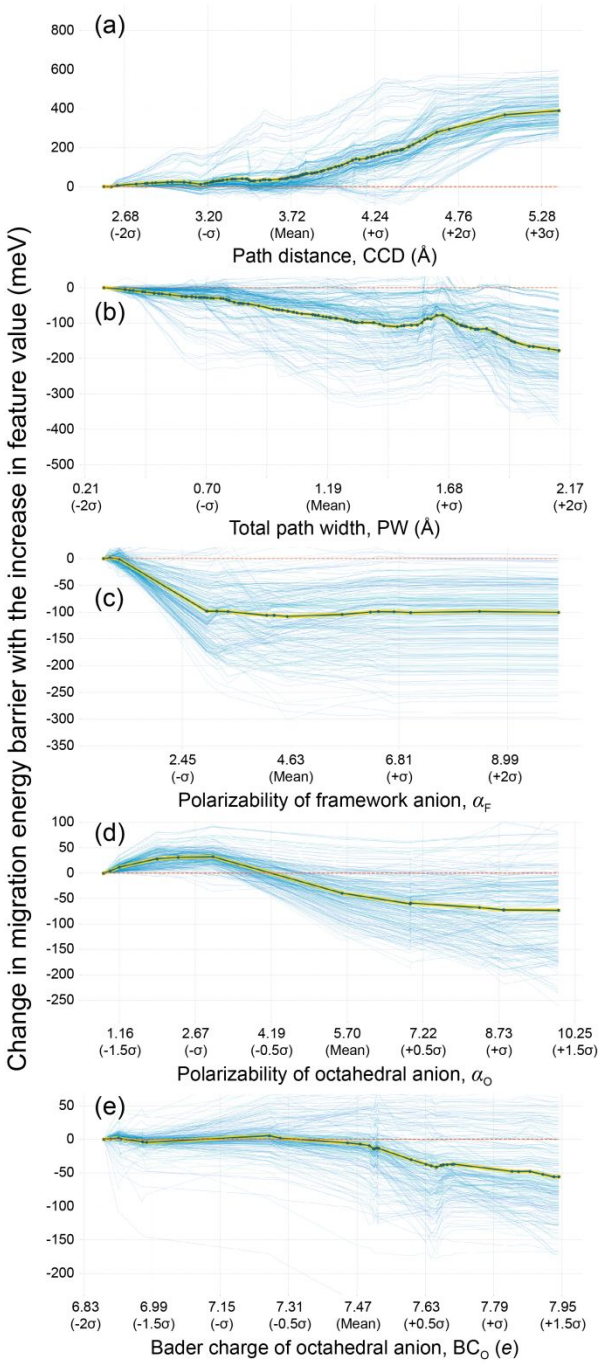

Figure 8. Individual conditional expectation (ICE) plots for the features relevant for vacancy migration: (a) path distance, CCD, (b) total path width, PW, (c) polarizability of the framework anion, α_F, (d) polarizability of the octahedral anion, α_O, and (e) Bader charge of octahedral anion, BC_O. Blue lines represent the change in migration barrier for each migration path in the training dataset as the target feature is varied from its minimum to its maximum value. The bold line depicts the average of the migration barrier over all curves. σ denotes the standard deviation of a given feature within the training data.

Finally, Figure 8e shows that the migration barrier decreases with increasing BC_O, although the sensitivity to the barrier is negligible for small BC_O. Furthermore, the overall change in the barrier size across the full range of BC_O is the smallest of the 5 features investigated, consistent with the smaller feature importance percentages shown in Fig. 7.

Feature importance – interstitial migration. Figure 7b shows the feature importance analysis for interstitial dumbbell migration. Similar to vacancy migration, the width of the migration channel (PW) plays an important role in determining the migration barrier for interstitials. PW is the most important feature, comprising 49% of the total importance for interstitial migration, surpassing its importance (28%) for vacancy migration. The greater importance played by the path geometry for interstitial migration likely reflects a sensitivity to the greater lattice strain induced by interstitial ions compared to that of vacancies (i.e., atom crowding is exacerbated in the presence of interstitials). Different from the case for vacancy migration, the path distance (CCD), which appeared as the most important feature for vacancy migration, does not appear as an important feature to describe the migration of the interstitial dumbbell. (Indeed, CCD was not identified as a necessary feature in training the ML model.)

The formation energy of the interstitial dumbbell (E_f) and the bond ionicity between the cation and chalcogen anion ($I_{C\text{-}Ch}$) appear as the second- and third-most important features, comprising 35% and 16% of the relative importance, respectively. It is noteworthy that the formation energy emerges as a relevant feature, as it is not widely recognized as a property that correlates with the migration barrier of interstitials. (Rather, E_f is well-known to impact the concentration of interstitials.) Its identification highlights a benefit of the present ML analysis in pinpointing overlooked features. E_f includes contributions from lattice strain, as well as from alterations in the bonding network of the interstitial. As discussed above, strain dependence was also cited as an explanation for the greater importance of the path width in interstitial vs. vacancy migration. Consequently, it may be hypothesized that E_f is a relevant feature for interstitial migration due to its similar dependence on lattice strain.

Figure S3 presents ICE plots for the important features associated with interstitial migration. Regarding the dependence on PW, figure S3a shows that the migration barrier is approximately insensitive to PW for channel widths less than 1.7 Å. The barrier then decreases for increasingly larger PW. The fact that the PW must be larger than a threshold value (~1.7 Å) to observe a reduction in the barrier suggests that the interstitial exhibits a characteristic size that the channel must accommodate to allow for enhanced cation mobility. Regarding the dependence on E_f, Figure S3b shows that the migration barrier generally increases with increasing E_f. This behavior is consistent with the previously-discussed notion that lattice strain is necessary to both form the interstitial and for it to migrate; the energy penalties associated with these strains impede cation mobility. Finally, Figure S3c illustrates a gradual increase in the barrier with increasing $I_{C\text{-}Ch}$.

Conclusion

This present study has employed ML to quantify the importance of several chemical, physical, and structural features on ion transport within a crystalline lattice. Adopting the anti-perovskite crystal structure as a model system, several ML algorithms were trained to predict ion migration barriers. The

algorithms were informed by a data set containing more than 600 barriers that were calculated in a consistent fashion using density functional theory. The training set is derived from 36 alkali metal chalco-halide anti-perovskites, and includes vacancy and interstitial migration mechanisms. Highly correlated (i.e., redundant) features were identified and eliminated from the analysis, thus maximizing the simplicity of the resulting models and minimizing overfitting. Using the most accurate algorithm, the feature combinations that yielded the most accurate predictions were identified. Finally, the relative importance of the features and their influence on ion transport were quantified using the mean decrease in impurity (MDI) and individual conditional expectation (ICE) plots.

This analysis correctly reiterates the importance of features that are known to influence mobility – for example, anion polarizability – but also identifies others whose importance is not widely recognized. Lattice properties such as hopping distance and channel width were observed to have the greatest influence on cation mobility. These features comprise 70% of the total feature importance for vacancy migration, and ~50% of the importance for interstitial migration. Individual conditional expectation analyses performed on these features showed that barriers decrease as hopping distance decreases and as channel width increases. Additional significant features include the anion polarizability (22% for vacancy migration) and the defect formation energy (35% for interstitial migration). The identification of the formation energy as a significant feature for interstitial migration is noteworthy because this feature is not widely recognized as one that influences mobility; rather, the formation energy is typically associated with the concentration of defects.

In sum, this analysis will facilitate the design of efficient solid electrolytes by reducing the multi-dimensional design space to a sub-set of properties that are the most important. Nevertheless, as this work specifically targets ion mobility in anti-perovskites, an important next step will be to generalize the results to other crystal structure classes. An example of an improvement that would facilitate application to a wider range of solids is the inclusion of dynamical phenomena such as lattice vibrations and poly-anion rotations within the feature set. In support of such a more general analysis, it should be noted that essentially all of the features that were used in the present study of APs are straightforward to evaluate (or obtain) for other categories of crystalline conductors. Moreover, several of the most important features identified here for vacancy migration have been discussed in the literature for other crystal systems, implying a degree of transferability of the present results.[19–23,44]

ASSOCIATED CONTENT

Supporting Information

Details regarding the descriptor set; Details regarding feature filtering; Machine-learning algorithms; Pearson correlation analysis for interstitial migration; List of descriptors in feature subsets; Predictability of single-feature models; ICE analysis for interstitial dumbbell migration; Complete dataset of the ion migration barriers and the associated features; Pearson correlation result.

AUTHOR INFORMATION

Corresponding Author

*E-mail: Donald.Siegel@austin.utexas.edu. Tel.: +1 512-471-0796.

Current address

[#]K.K.: Lawrence Livermore National Laboratory, Livermore, California, 94550, United States.
[#]D.J.S.: Walker Department of Mechanical Engineering, Texas Materials Institute, Oden Institute for Computational Engineering and Sciences, University of Texas at Austin, Austin, TX, 78712-1591, United States.

Author contributions

K.K. conducted the computational analysis of the project. All authors contributed to the drafting of the paper. D.J.S. conceived the project idea.

Conflicts of interest

There are no conflicts of interest to declare.

ACKNOWLEDGMENT

This work was supported as part of the Joint Center for Energy Storage Research (JCESR), an Energy Innovation Hub funded by the U.S. Department of Energy, Office of Science, Basic Energy Sciences.

REFERENCES

(1) Goodenough, J. B.; Kim, Y. Challenges for Rechargeable Li Batteries. *Chem. Mater.* **2010**, *22* (3), 587–603. https://doi.org/10.1021/cm901452z.

(2) Roth, E. P.; Orendorff, C. J. How Electrolytes Influence Battery Safety. *Electrochem. Soc. Interface* **2012**, *21* (2), 45–49. https://doi.org/10.1149/2.F04122if.

(3) Goodenough, J. B.; Singh, P. Review—Solid Electrolytes in Rechargeable Electrochemical Cells. *J. Electrochem. Soc.* **2015**, *162* (14), A2387–A2392. https://doi.org/10.1149/2.0021514jes.

(4) Monroe, C.; Newman, J. The Impact of Elastic Deformation on Deposition Kinetics at Lithium/Polymer Interfaces. *J. Electrochem. Soc.* **2005**, *152* (2), A396–A404. https://doi.org/10.1149/1.1850854.

(5) Lin, D.; Liu, Y.; Cui, Y. Reviving the Lithium Metal Anode for High-Energy Batteries. *Nat. Nanotechnol.* **2017**, *12* (3), 194–206. https://doi.org/10.1038/nnano.2017.16.

(6) Kamaya, N.; Homma, K.; Yamakawa, Y.; Hirayama, M.; Kanno, R.; Yonemura, M.; Kamiyama, T.; Kato, Y.; Hama, S.; Kawamoto, K.; et al. A Lithium Superionic Conductor. *Nat. Mater.* **2011**, *10* (9), 682–686. https://doi.org/10.1038/nmat3066.

(7) Deiseroth, H.-J.; Kong, S. T.; Eckert, H.; Vannahme, J.; Reiner, C.; Zaiß, T.; Schlosser, M. Li_6PS_5X: A Class of Crystalline Li-Rich Solids with an Unusually High Li^+ Mobility. *Angew. Chemie - Int. Ed.* **2008**, *47* (4), 755–758. https://doi.org/10.1002/anie.200703900.

(8) Murugan, R.; Thangadurai, V.; Weppner, W. Fast Lithium Ion Conduction in Garnet-Type $Li_7La_3Zr_2O_{12}$. *Angew. Chemie - Int. Ed.* **2007**, *46* (41), 7778–7781. https://doi.org/10.1002/anie.200701144.

(9) Aono, H.; Sugimoto, E.; Sadaoka, Y.; Imanaka, N.; Adachi, G. Ionic Conductivity of Solid Electrolytes Based on Lithium Titanium Phosphate. *J. Electrochem. Soc.* **1990**, *137* (4), 1023–1027. https://doi.org/10.1149/1.2086597.

(10) Boukamp, B. A.; Huggins, R. A. Fast Ionic Conductivity in Lithium Nitride. *Mater. Res. Bull.* **1978**, *13* (1), 23–32. https://doi.org/10.1016/0025-5408(78)90023-5.

(11) Inaguma, Y.; Liquan, C.; Itoh, M.; Nakamura, T.; Uchida, T.; Ikuta, H.; Wakihara, M. HIGH IONIC CONDUCTIVITY IN LITHIUM LANTHANUM TITANATE. *Solid State Commun.* **1993**, *86* (10), 689–693. https://doi.org/10.1016/0038-1098(93)90841-A.

(12) Bachman, J. C.; Muy, S.; Grimaud, A.; Chang, H. H.; Pour, N.; Lux, S. F.; Paschos, O.; Maglia, F.; Lupart, S.; Lamp, P.; et al. Inorganic Solid-State Electrolytes for Lithium Batteries: Mechanisms and Properties Governing Ion Conduction. *Chem.*

Rev. **2016**, *116* (1), 140–162. https://doi.org/10.1021/acs.chemrev.5b00563.

(13) Richards, W. D.; Miara, L. J.; Wang, Y.; Kim, J. C.; Ceder, G. Interface Stability in Solid-State Batteries. *Chem. Mater.* **2016**, *28* (1), 266–273. https://doi.org/10.1021/acs.chemmater.5b04082.

(14) Cheng, E. J.; Sharafi, A.; Sakamoto, J. Intergranular Li Metal Propagation through Polycrystalline $Li_{6.25}Al_{0.25}La_3Zr_2O_{12}$ Ceramic Electrolyte. *Electrochim. Acta* **2017**, *223*, 85–91. https://doi.org/10.1016/j.electacta.2016.12.018.

(15) Zhu, Y.; He, X.; Mo, Y. Origin of Outstanding Stability in the Lithium Solid Electrolyte Materials: Insights from Thermodynamic Analyses Based on First-Principles Calculations. *ACS Appl. Mater. Interfaces* **2015**, *7* (42), 23685–23693. https://doi.org/10.1021/acsami.5b07517.

(16) Jain, A.; Ong, S. P.; Hautier, G.; Chen, W.; Richards, W. D.; Dacek, S.; Cholia, S.; Gunter, D.; Skinner, D.; Ceder, G.; et al. Commentary: The Materials Project: A Materials Genome Approach to Accelerating Materials Innovation. *APL Mater.* **2013**, *1* (1), 011002. https://doi.org/10.1063/1.4812323.

(17) Wakamura, K. Roles of Phonon Amplitude and Low-Energy Optical Phonons on Superionic Conduction. *Phys. Rev. B - Condens. Matter Mater. Phys.* **1997**, *56* (18), 11593–11599.

(18) Muy, S.; Bachman, J. C.; Giordano, L.; Chang, H.; Abernathy, D. L.; Bansal, D.; Delaire, O.; Hori, S.; Kanno, R.; Maglia, F.; et al. Tuning Mobility and Stability of Lithium Ion Conductors Based on Lattice Dynamics. *Energy Environ. Sci.* **2018**, *11* (4), 850–859. https://doi.org/10.1039/C7EE03364H.

(19) Wuensch, B. J.; Vasilos, T. Diffusion of Transition Metal Ions in Single-Crystal MgO. *J. Chem. Phys.* **1962**, *36* (11), 2917–2922. https://doi.org/10.1063/1.1732402.

(20) Brüesch, P.; Pietronero, L.; Strässler, S.; Zeller, H. R. Brownian Motion in a Polarizable Lattice: Application to Superionic Conductors. *Phys. Rev. B* **1977**, *15* (10), 4631–4637. https://doi.org/10.1103/PhysRevB.15.4631.

(21) Aidhy, D. S.; Sinnott, S. B.; Wachsman, E. D.; Phillpot, S. R. Effect of Ionic Polarizability on Oxygen Diffusion in δ-Bi_2O_3 from Atomistic Simulation. *Ionics (Kiel).* **2010**, *16* (4), 297–303. https://doi.org/10.1007/s11581-010-0430-5.

(22) Kraft, M. A.; Culver, S. P.; Calderon, M.; Böcher, F.; Krauskopf, T.; Senyshyn, A.; Dietrich, C.; Zevalkink, A.; Janek, J.; Zeier, W. G. Influence of Lattice Polarizability on the Ionic Conductivity in the Lithium Superionic Argyrodites Li_6PS_5X (X = Cl, Br, I). *J. Am. Chem. Soc.* **2017**, *139* (31), 10909–10918. https://doi.org/10.1021/jacs.7b06327.

(23) Takahashi, T.; Nagagiri, K.; Iwadate, Y.; Utsuno, F.; Yamaguchi, H.; Ohkubo, T. Li Conduction Pathways in Solid-State Electrolytes: Insights from Dynamics and Polarizability. *Chem. Phys. Lett.* **2018**, *698*, 234–239. https://doi.org/10.1016/j.cplett.2018.03.014.

(24) Rong, Z.; Malik, R.; Canepa, P.; Sai Gautam, G.; Liu, M.; Jain, A.; Persson, K.; Ceder, G. Materials Design Rules for Multivalent Ion Mobility in Intercalation Structures. *Chem. Mater.* **2015**, *27* (17), 6016–6021. https://doi.org/10.1021/acs.chemmater.5b02342.

(25) Wang, Y.; Richards, W. D.; Ong, S. P.; Miara, L. J.; Kim, J. C.; Mo, Y.; Ceder, G. Design Principles for Solid-State Lithium Superionic Conductors. *Nat. Mater.* **2015**, *14* (10), 1026–1031. https://doi.org/10.1038/nmat4369.

(26) Ong, S. P.; Mo, Y.; Richards, W. D.; Miara, L.; Lee, H. S.; Ceder, G. Phase Stability, Electrochemical Stability and Ionic Conductivity of the $Li_{10\pm1}MP_2X_{12}$ (M = Ge, Si, Sn, Al or P, and X = O, S or Se) Family of Superionic Conductors. *Energy Environ. Sci.* **2013**, *6* (1), 148–156. https://doi.org/10.1039/C2EE23355J.

(27) Canepa, P.; Bo, S. H.; Sai Gautam, G.; Key, B.; Richards, W. D.; Shi, T.; Tian, Y.; Wang, Y.; Li, J.; Ceder, G. High Magnesium Mobility in Ternary Spinel Chalcogenides. *Nat. Commun.* **2017**, *8*, 1759. https://doi.org/10.1038/s41467-017-01772-1.

(28) Anslyn, E. V.; Dougherty, D. A. *Modern Physical Organic Chemistry*; University Science Books: Sausalito, Ca, 2006.

(29) Jansen, M. Volume Effect or Paddle-Wheel Mechanism - Fast Alkali-Metal Ionic Conduction in Solids with Rotationally Disordered Complex Anions. *Angew. Chemie Int. Ed. English* **1991**, *30* (12), 1547–1558. https://doi.org/10.1080/07370024.2011.601670.

(30) Verdal, N.; Udovic, T. J.; Stavila, V.; Tang, W. S.; Rush, J. J.; Skripov, A. V. Anion Reorientations in the Superionic Conducting Phase of $Na_2B_{12}H_{12}$. *J. Phys. Chem. C* **2014**, *118* (31), 17483–17489. https://doi.org/10.1021/jp506252c.

(31) Varley, J. B.; Kweon, K.; Mehta, P.; Shea, P.; Heo, T. W.; Udovic, T. J.; Stavila, V.; Wood, B. C. Understanding Ionic Conductivity Trends in Polyborane Solid Electrolytes from Ab Initio Molecular Dynamics. *ACS Energy Lett.* **2017**, *2* (1), 250–255. https://doi.org/10.1021/acsenergylett.6b00620.

(32) Kweon, K. E.; Varley, J. B.; Shea, P.; Adelstein, N.; Mehta, P.; Heo, T. W.; Udovic, T. J.; Stavila, V.; Wood, B. C. Structural, Chemical, and Dynamical Frustration: Origins of Superionic Conductivity in Closo -Borate Solid Electrolytes. *Chem. Mater.* **2017**, *29* (21), 9142–9153. https://doi.org/10.1021/acs.chemmater.7b02902.

(33) Fang, H.; Wang, S.; Liu, J.; Sun, Q.; Jena, P. Superhalogen-Based Lithium Superionic Conductors. *J. Mater. Chem. A* **2017**, *5* (26), 13373–13381. https://doi.org/10.1039/C7TA01648D.

(34) Song, A.; Turcheniuk, K.; Leisen, J.; Xiao, Y.; Meda, L.; Borodin, O.; Yushin, G. Understanding Li-Ion Dynamics in Lithium Hydroxychloride (Li_2OHCl) Solid State Electrolyte via Addressing the Role of Protons. *Adv. Energy Mater.* **2020**, *10* (8), 1903480. https://doi.org/10.1002/aenm.201903480.

(35) Smith, J. G.; Siegel, D. J. Low-Temperature Paddlewheel Effect in Glassy Solid Electrolytes. *Nat. Commun.* **2020**, *11* (1), 1483. https://doi.org/10.1038/s41467-020-15245-5.

(36) Wang, F.; Evans, H. A.; Kim, K.; Yin, L.; Li, Y.; Tsai, P.-C.; Liu, J.; Lapidus, S. H.; Brown, C. M.; Siegel, D. J.; et al. Dynamics of Hydroxyl Anions Promotes Lithium Ion Conduction in Antiperovskite Li_2OHCl. *Chem. Mater.* **2020**, *32* (19), 8481–8491. https://doi.org/10.1021/acs.chemmater.0c02602.

(37) Kim, K.; Siegel, D. J. Correlating Lattice Distortions, Ion Migration Barriers, and Stability in Solid Electrolytes. *J. Mater. Chem. A* **2019**, *7* (7), 3216–3227. https://doi.org/10.1039/C8TA10989C.

(38) Zhang, Z.; Shao, Y.; Lotsch, B.; Hu, Y.-S.; Li, H.; Janek, J.; Nazar, L. F.; Nan, C.; Maier, J.; Armand, M.; et al. New Horizons for Inorganic Solid State Ion Conductors. *Energy Environ. Sci.* **2018**, *11* (8), 1945–1976. https://doi.org/10.1039/C8EE01053F.

(39) Liu, Y.; Zhao, T.; Ju, W.; Shi, S.; Shi, S.; Shi, S. Materials Discovery and Design Using Machine Learning. *J. Mater.* **2017**, *3* (3), 159–177. https://doi.org/10.1016/j.jmat.2017.08.002.

(40) Fujimura, K.; Seko, A.; Koyama, Y.; Kuwabara, A.; Kishida, I.; Shitara, K.; Fisher, C. A. J.; Moriwake, H.; Tanaka, I. Accelerated Materials Design of Lithium Superionic Conductors Based on First-Principles Calculations and Machine Learning Algorithms. *Adv. Energy Mater.* **2013**, *3* (8), 980–985. https://doi.org/10.1002/aenm.201300060.

(41) Jalem, R.; Nakayama, M.; Kasuga, T. An Efficient Rule-Based Screening Approach for Discovering Fast Lithium Ion Conductors Using Density Functional Theory and Artificial Neural Networks. *J. Mater. Chem. A* **2014**, *2* (3), 720–734. https://doi.org/10.1039/c3ta13235h.

(42) Jalem, R.; Kimura, M.; Nakayama, M.; Kasuga, T. Informatics-Aided Density Functional Theory Study on the Li Ion Transport of Tavorite-Type LiMTO4F (M3+-T5+, M2+-T6+). *J. Chem. Inf. Model.* **2015**, *55* (6), 1158–1168. https://doi.org/10.1021/ci500752n.

(43) Kireeva, N.; Pervov, V. S. Materials Space of Solid-State Electrolytes: Unraveling Chemical Composition-Structure-Ionic Conductivity Relationships in Garnet-Type Metal Oxides Using Cheminformatics Virtual Screening Approaches. *Phys. Chem. Chem. Phys.* **2017**, *19* (31), 20904–20918. https://doi.org/10.1039/c7cp00518k.

(44) Sendek, A. D.; Yang, Q.; Cubuk, E. D.; Duerloo, K.-A. N.; Cui, Y.; Reed, E. J. Holistic Computational Structure Screening of More than 12 000 Candidates for Solid Lithium-Ion Conductor Materials. *Energy Environ. Sci.* **2017**, *10* (1), 306–320. https://doi.org/10.1039/C6EE02697D.

(45) Jalem, R.; Kanamori, K.; Takeuchi, I.; Nakayama, M.; Yamasaki, H.; Saito, T. Bayesian-Driven First-Principles Calculations for Accelerating Exploration of Fast Ion Conductors for Rechargeable Battery Application. *Sci. Rep.* **2018**, *8* (1), 5845.

https://doi.org/10.1038/s41598-018-23852-y.
(46) Katcho, N. A.; Carrete, J.; Reynaud, M.; Rousse, G.; Casas-Cabanas, M.; Mingo, N.; Rodríguez-Carvajal, J.; Carrasco, J. An Investigation of the Structural Properties of Li and Na Fast Ion Conductors Using High-Throughput Bond-Valence Calculations and Machine Learning. *J. Appl. Crystallogr.* **2019**, *52* (1), 148–157. https://doi.org/10.1107/S1600576718018484.
(47) Kim, K. Computational Discovery of Solid Electrolytes for Batteries: Interfacial Phenomena and Ion Mobility. PhD Thesis, University of Michigan, Ann Arbor, 2020.
(48) Pedregosa, F.; Varoquaux, G.; Gramfort, A.; Michel, V.; Thirion, B.; Grisel, O.; Blondel, M.; Prettenhofer, P.; Weiss, R.; Dubourg, V.; et al. Scikit-Learn: Machine Learning in Python. *J. Mach. Learn. Res.* **2011**, *12*, 2825–2830. https://doi.org/10.1007/s13398-014-0173-7.2.
(49) Fujii, S.; Gao, S.; Tassel, C.; Zhu, T.; Broux, T.; Okada, K.; Miyahara, Y.; Kuwabara, A.; Kageyama, H. Alkali-Rich Antiperovskite M_3FCh (M = Li, Na; Ch = S, Se, Te): The Role of Anions in Phase Stability and Ionic Transport. *J. Am. Chem. Soc.* **2021**, *143* (28), 10668–10675. https://doi.org/10.1021/jacs.1c04260.
(50) Kim, K.; Li, Y.; Tsai, P.-C.; Wang, F.; Son, S.-B.; Chiang, Y.-M.; Siegel, D. J. Exploring the Synthesis of Alkali Metal Anti-Perovskites. *Chem. Mater.* **2022**. https://doi.org/10.1021/acs.chemmater.1c02150.
(51) Bishop, C. M. *Pattern Recognition and Machine Learning*; Springer: New York, NY, 2006.
(52) Theodoridis, S.; Koutroumbas, K. *Pattern Recognition*, 4th ed.; Academin Press: Burlington, MA, 2008.
(53) Pearson, E. W.; Jackson, M. D.; Gordon, R. G. A Theoretical Model for the Index of Refraction of Simple Ionic Crystals. *J. Phys. Chem.* **1984**, *88* (1), 119–128. https://doi.org/10.1021/j150645a030.
(54) Shannon, R. D. Revised Effective Ionic Radii and Systematic Studies of Interatomic Distances in Halides and Chalcogenides. *Acta Crystallogr. Sect. A* **1976**, *32* (5), 751–767. https://doi.org/10.1107/S0567739476001551.
(55) Coursey, J. S.; Schwab, D. J.; Tsai, J. J.; Dragoset, R. A. *Atomic Weights and Isotopic Compositions with Relative Atomic Masses*; National Institute of Standards and Technology (NIST) Physical Measurement Laboratory, 2015.
(56) Pauling, L. THE NATURE OF THE CHEMICAL BOND. IV. THE ENERGY OF SINGLE BONDS AND THE RELATIVE ELECTRONEGATIVITY OF ATOMS. *J. Am. Chem. Soc.* **1932**, *54* (9), 3570–3582. https://doi.org/10.1021/ja01348a011.
(57) Allred, A. L. Electronegativity Values from Thermochemical Data. *J. Inorg. Nucl. Chem.* **1961**, *17* (3–4), 215–221. https://doi.org/10.1016/0022-1902(61)80142-5.
(58) Bader, R. F. W. *Atoms in Molecules: A Quantum Theory*; Oxford University Press: New York, 1990.
(59) Henkelman, G.; Arnaldsson, A.; Jónsson, H. A Fast and Robust Algorithm for Bader Decomposition of Charge Density. *Comput. Mater. Sci.* **2006**, *36* (3), 354–360. https://doi.org/10.1016/j.commatsci.2005.04.010.
(60) Sanville, E.; Kenny, S. D.; Smith, R.; Henkelman, G. Improved Grid-Based Algorithm for Bader Charge Allocation. *J. Comput. Chem.* **2007**, *28* (5), 899–908. https://doi.org/10.1002/jcc.20575.
(61) Tang, W.; Sanville, E.; Henkelman, G. A Grid-Based Bader Analysis Algorithm without Lattice Bias. *J. Phys. Condens. Matter* **2009**, *21* (8), 084204. https://doi.org/10.1088/0953-8984/21/8/084204.
(62) Goldschmidt, V. M. Die Gesetze Der Krystallochemie. *Naturwissenschaften* **1926**, *14* (21), 477–485. https://doi.org/10.1007/BF01507527.
(63) Willems, T. F.; Rycroft, C. H.; Kazi, M.; Meza, J. C.; Haranczyk, M. Algorithms and Tools for High-Throughput Geometry-Based Analysis of Crystalline Porous Materials. *Microporous Mesoporous Mater.* **2012**, *149* (1), 134–141. https://doi.org/10.1016/j.micromeso.2011.08.020.
(64) Köhler, U.; Herzig, C. On the Correlation between Self-Diffusion and the Low-Frequency LA ⅔ ⟨ 111 ⟩ Phonon Mode in b . c . c . Metals. *Philos. Mag. A* **1988**, *58* (5), 769–786. https://doi.org/10.1080/01418618808209952.
(65) Zhu, Y.; He, X.; Mo, Y. First Principles Study on Electrochemical and Chemical Stability of Solid Electrolyte–Electrode Interfaces in All-Solid-State Li-Ion Batteries. *J. Mater. Chem. A* **2016**, *4* (9), 3253–3266. https://doi.org/10.1039/C5TA08574H.
(66) Van de Walle, C. G.; Neugebauer, J. First-Principles Calculations for Defects and Impurities: Applications to III-Nitrides. *J. Appl. Phys.* **2004**, *95* (8), 3851–3879. https://doi.org/10.1063/1.1682673.
(67) Rodgers, J. L.; Nicewander, W. A. Thirteen Ways to Look at the Correlation Coefficient. *Am. Stat.* **1988**, *42* (1), 59–66. https://doi.org/10.1080/00031305.1988.10475524.
(68) Hoerl, A. E.; Kennard, R. W. Ridge Regression: Biased Estimation for Nonorthogonal Problems. *Technometrics* **1970**, *12* (1), 55–67.
(69) Tibshirani, R. Regression Shrinkage and Selection via the Lasso. *J. R. Stat. Soc. Ser. B (Statistical Methodol.* **1996**, *58* (1), 267–288.
(70) Zou, H.; Hastie, T. Regression and Variable Selection via the Elastic Net. *J. R. Stat. Soc. Ser. B (Statistical Methodol.* **2005**, *67* (2), 301–320. https://doi.org/10.1111/j.1467-9868.2005.00503.x.
(71) Mackay, D. J. C. Bayesian Methods for Backpropagation Networks. In *Models of Neural Networks III*; Domany, E., van Hemmen, J. L., Schulten, K., Eds.; Springer, 1994; pp 211–254.
(72) Huber, P. J. Robust Estimation of a Location Parameter. *Ann. Math. Stat.* **1964**, *35* (1), 73–101. https://doi.org/10.1214/aoms/1177703732.
(73) Crammer, K.; Dekel, O.; Keshet, J.; Shalev-Shwartz, S.; Singer, Y. Online Passive-Aggressive Algorithms. *J. Mach. Learn. Res.* **2006**, *7*, 551–585.
(74) Drucker, H.; Burges, C. J. C.; Kaufman, L.; Smola, A.; Vapnik, V. Support Vector Regression Machines. In *Neural Information Processing Systems*; Mozer, M. C., Joradn, J. I., Petsche, T., Eds.; MIT Press: Cambridge, MA, 1997; Vol. 9, pp 155–161.
(75) Chang, C.-C.; Lin, C.-J. LIBSVM: A Library for Support Vector Machines. *ACM Trans. Intell. Syst. Technol.* **2011**, *2* (3), 27. https://doi.org/10.1145/1961189.1961199.
(76) Fan, R.-E.; Chang, K.-W.; Hsieh, C.-J.; Wang, X.-R.; Lin, C.-J. LIBLINEAR: A Library for Large Linear Classification. *J. Mach. Learn. Res.* **2008**, *9*, 1871–1874.
(77) Schölkopf, B.; Smola, A. J.; Williamson, R. C.; Bartlett, P. L. New Support Vector Algorithms. *Neural Comput.* **2000**, *12*, 1207–1245.
(78) Breiman, L.; Friedman, J. H.; Olshen, R. A.; Stone, C. J. *Classification and Regression Trees*; Chapman and Hall/CRC: Boca Raton, FL, 1984.
(79) Bramer, M. *Principles of Data Mining*, 2nd ed.; Springer-Verlag: London, 2007. https://doi.org/10.1007/978-1-4471-4884-5_1.
(80) Breiman, L. Bagging Predictors. *Mach. Learn.* **1996**, *24* (2), 123–140. https://doi.org/10.1007/BF00058655.
(81) Tin Kam Ho. Random Decision Forests. In *Proceedings of 3rd International Conference on Document Analysis and Recognition*; IEEE Comput. Soc. Press, 1995; Vol. 1, pp 278–282. https://doi.org/10.1109/ICDAR.1995.598994.
(82) Breiman, L. Random Forests. *Mach. Learn.* **2001**, *45* (1), 5–32. https://doi.org/10.1023/A:1010933404324.
(83) Geurts, P.; Ernst, D.; Wehenkel, L. Extremely Randomized Trees. *Mach. Learn.* **2006**, *63* (1), 3–42. https://doi.org/10.1007/s10994-006-6226-1.
(84) Freund, Y.; Schapire, R. E. A Decision-Theoretic Generalization of On-Line Learning and an Application to Boosting. *J. Comput. Syst. Sci.* **1997**, *55* (1), 119–139. https://doi.org/10.1006/jcss.1997.1504.
(85) Drucker, H. Improving Regressors Using Boosting Techniques. In *Proceedings of the 14th International Conference on Machine Learning*; 1997; pp 107–115.
(86) Friedman, J. H. . Greedy Function Approximation: A Gradient Boosting Machine. *Ann. Stat.* **2001**, *29* (5), 1189–1232.
(87) Kohavi, R. A Study of Cross-Validation and Bootstrap for Accuracy Estimation and Model Selection. *Proc. 14th Int. Jt. Conf. Artif. Intell.* **1995**, *2*, 1137–1143.
(88) Kohavi, R.; John, G. H. Wrappers for Feature Subset Selection. *Artif. Intell.* **1997**, *97* (1–2), 273–324. https://doi.org/10.1016/S0004-3702(97)00043-X.
(89) Goldstein, A.; Kapelner, A.; Bleich, J.; Pitkin, E. Peeking Inside the Black Box: Visualizing Statistical Learning With Plots of

Individual Conditional Expectation. *J. Comput. Graph. Stat.* **2015**, *24* (1), 44–65. https://doi.org/10.1080/10618600.2014.907095.

(90) PDPbox. *GitHub* (https://github.com/SauceCat/PDPbox), Accessed June 13, 2019.